

Stimulated Raman scattering tomography for rapid three-dimensional chemical imaging of cells and tissue

Weiqi Wang¹ and Zhiwei Huang^{1*}

National University of Singapore, College of Design and Engineering, Optical Bioimaging Laboratory, Department of Biomedical Engineering, Singapore

Abstract. Three-dimensional (3D) imaging is essential for understanding intricate biological and biomedical systems, yet live cell and tissue imaging applications still face challenges due to constrained imaging speed and strong scattering in turbid media. Here, we present a unique phase-modulated stimulated Raman scattering tomography (PM-SRST) technique to achieve rapid label-free 3D chemical imaging in cells and tissue. To accomplish PM-SRST, we utilize a spatial light modulator to electronically manipulate the focused Stokes beam along the needle Bessel pump beam for SRS tomography without the need for mechanical z scanning. We demonstrate the rapid 3D imaging capability of PM-SRST by real-time monitoring of 3D Brownian motion of polystyrene beads in water with 8.5 Hz volume rate, as well as the instant biochemical responses to acetic acid stimulants in MCF-7 cells. Further, combining the Bessel pump beam with a longer wavelength Stokes beam (NIR-II window) provides a superior scattering resilient ability in PM-SRST, enabling rapid tomography in deeper tissue areas. The PM-SRST technique provides \sim twofold enhancement in imaging depth in highly scattering media (e.g., polymer beads phantom and biotissue like porcine skin and brain tissue) compared with conventional point-scan SRS. We also demonstrate the rapid 3D imaging ability of PM-SRST by observing the dynamic diffusion and uptake processes of deuterium oxide molecules into plant roots. The rapid PM-SRST developed can be used to facilitate label-free 3D chemical imaging of metabolic activities and functional dynamic processes of drug delivery and therapeutics in live cells and tissue.

Keywords: stimulated Raman scattering tomography; deep tissue Raman imaging; spatial light modulation.

Received Sep. 8, 2023; revised manuscript received Dec. 30, 2023; accepted for publication Jan. 25, 2024; published online Feb. 15, 2024.

© The Authors. Published by SPIE and CLP under a Creative Commons Attribution 4.0 International License. Distribution or reproduction of this work in whole or in part requires full attribution of the original publication, including its DOI.

[DOI: [10.1117/1.AP.6.2.026001](https://doi.org/10.1117/1.AP.6.2.026001)]

1 Introduction

Volumetric tissue imaging based on multimodal microscopy techniques [e.g., confocal microscopy, multiphoton microscopy, harmonic generation microscopy, and coherent Raman scattering (CRS) microscopy]^{1–5} provides a global visualization of three-dimensional (3D) complex biosystems with more comprehensive information about the sample as compared to 2D imaging, which has been proven to be of great value to further understand the fundamental mechanisms of live tissue and cell biology and biochemistry (e.g., in the studies of cancer

diagnosis and therapy, drug delivery, cell metabolisms, neuron functions, and developmental biology^{6–10}). Among the nonlinear optical imaging techniques, CRS [i.e., stimulated Raman scattering (SRS) and anti-Stokes Raman scattering (CARS)] microscopy is an optical vibrational spectroscopy imaging technique with high biochemical specificity for label-free chemical imaging in tissue and cells.¹¹ With the advantages of the linear relationship between Raman intensity and concentration of the target molecules without the nonresonant background interference, SRS microscopy is particularly powerful for quantitative biomolecular imaging in biological and biomedical systems.^{4,5} In SRS imaging, the two near-infrared (NIR) ultrafast laser beams (termed as pump, ω_p , and Stokes, ω_s) with the

*Address all correspondence to Zhiwei Huang, biehw@nus.edu.sg

wavelength difference of ~ 200 nm are used and temporally and spatially overlapped and focused onto the sample for SRS imaging. Through tuning the beating frequency of the two-color laser beams to match the specific vibrational frequency of the target molecules in the sample (i.e., $\omega_p - \omega_s =$ vibrational frequency of the target molecules), the CRS process occurs along the phase-matching direction for SRS imaging with biomolecular contrast.¹¹ To acquire the 3D information of the sample, the common method is implemented with a series of 2D scans across different depths of the sample by mechanical motion of the objective lens or sample stage along the z direction, but such a mechanical scanning suffers from inertia artifacts with mechanical refocusing for 3D image co-registrations,¹² resulting in compromised 3D imaging speed and quality. Besides the constrained scanning speed in the z direction, the strong light-scattering effect inherent in biological/biomedical specimens further impedes rapid imaging in deep tissue areas. Strategies based on Bessel light beams have been proposed for 3D chemical imaging, such as optical projection tomography (OPT)¹³ coupled with Bessel pump and Stokes beams, in which the SRS 3D images are retrieved from a series of 2D images at multiple projections. However, OPT-based SRS 3D imaging requires the mechanical rotation of the sample, unsuited for rapid *in vivo* biological/biomedical applications. Optical beating tomography (OBT) provides an alternative avenue for deep-tissue imaging,¹⁴ in which the SRS 3D information is encoded by employing the Bessel beam beatings in the frequency domain, and the volumetric structure is retrieved by implementing the Fourier transform. The prolonged Bessel beating beams used, associated with the multiple beating modulations required, may degrade the signal level and also constrain the 3D imaging speed.

In this work, we present a unique phase-modulated stimulated Raman scattering tomography (PM-SRST) technique for rapid 3D chemical imaging in living cells and tissue. To achieve the mechanical scan-free z sectioning in PM-SRST, we apply a spatial light modulator (SLM) to manipulate the axial position of the focused Gaussian Stokes beam along the needle Bessel pump beam in the sample for SRST imaging. PM-SRST facilitates the direct acquisition of 3D sample information in the spatial domain, without necessitating postprocessing procedures. We have derived and analyzed the unique Bessel beam-based PM-SRST imaging method theoretically and also built the PM-SRST imaging system to experimentally demonstrate its capability for rapid label-free volumetric chemical imaging on a variety of samples [e.g., Brownian motion of polymer beads in water, diffusion and uptake processes of deuterium oxide (D_2O) in the plant root, and breast cancer cell response to acetic acid]. We have also demonstrated the utility of the PM-SRST technique for improving both the lateral resolution and imaging depth of SRS 3D imaging of biotissues.

2 Materials and Methods

2.1 Working Principle of PM-SRST

In SRS imaging, the sample is illuminated by the collinear pump and Stokes beams under a tight focus through a high numerical aperture (NA) objective lens. The SRS signal generated is proportional to the product of the pump and Stokes beam intensities.^{4,5} In PM-SRST, the pump light is converted into a Bessel beam by using an axicon and is focused onto the sample,

in which the intensity distribution in the sample space is as follows:¹⁵

$$I_p(r, z) = I_{p0} \frac{2\pi kz}{\cos \alpha} \sin^2 \alpha \exp \left[-2 \left(\frac{z \tan \alpha}{\omega_p} \right)^2 \right] |J_0(kr \sin \alpha)|^2, \quad (1)$$

where r and z are the coordinates in the lateral and longitudinal directions, respectively. I_{p0} is the on-axis intensity of the incident Gaussian pump beam. k is the wave vector, and α is the angle between the vector normal to the conical surface of the axicon and the z axis, i.e., $\alpha \cong \frac{n_a - n_s}{n_s} \frac{\pi - \beta}{2}$, where n_a is the refractive index of the axicon, n_s is the one of the surrounding media (e.g., air), and β is the apex angle of the axicon. ω_p is the waist of the incident Gaussian pump beam and J_0 is the zeroth-order Bessel function of the first kind.

The Gaussian Stokes beam is focused onto the sample as an Airy spot under the high NA objective lens, in which the intensity distribution is $I_s(r, z) = I_{s0} \exp(\frac{-2r^2}{\omega_s(z)^2})$, where I_{s0} is the on-axis intensity of the incident Gaussian Stokes beam and ω_s is the waist of the Stokes beam. Hence, the SRS intensity at position z is¹³

$$I_{SRS} = C_0 \text{Im}(\chi^{(3)}) I_p(r, z) I_s(r, z) \Delta L, \quad (2)$$

where C_0 is a constant, and $\text{Im}(\chi^{(3)})$ is the imaginary part of the third-order nonlinear susceptibility $\chi^{(3)}$. $I_p(r, z)$ and $I_s(r, z)$ are the intensities of the pump and Stokes beams at positions z , respectively. ΔL is the superposition length of the Gaussian Stokes and Bessel pump beams.

To control the axial position of the focused Stokes spot in the sample for depth-resolved SRS imaging, we change the divergence angle of the incident Stokes beam at the Fourier plane of the system through changing the phase patterns of the Stokes beam via an SLM. We can calculate the optical path difference (OPD) between the incident plane wave and the spherical wavefront to determine the axial position of the focal spot away from the focal plane of the lens. According to the Gaussian thin lens formula,¹⁶ the relationship between the axial position of the incident point source and the focus is as follows:

$$\frac{1}{s} + \frac{1}{\Delta z + f} = \frac{1}{f}, \quad (3)$$

where f is the focal length of the first lens after the SLM, s is the distance of the point source away from the lens, and Δz is the displacement of the focal spot from the focus of the lens. As such, the OPD between the spherical and the plane wavefront can be calculated as

$$\text{OPD} = (s - f) - \sqrt{(s - f)^2 - r_F^2}, \quad (4)$$

where r_F is the radial coordinate on the Fourier plane. Under the paraxial condition, we can make Taylor expansion for Eq. (4) and obtain the relationship between the Δz and the modulation phase Δp (OPD multiplied by wave vector k),

$$\Delta z = \frac{2f^2 \Delta p}{r_F^2 k}. \quad (5)$$

By substituting Eq. (5) into Eq. (2), we obtain the relationship between the SRS intensity on sample and Δz as follows:

$$I_{\text{SRS}} = C_0 \text{Im}(\chi^{(3)}) I_p(r, z) I_S \left(r, \frac{\Delta z}{M^2} + f_{\text{obj}} \right) \Delta L, \quad (6)$$

where M is the system magnification and f_{obj} is the focal length of the objective lens. Hence, Eq. (6) serves as the basis in PM-SRST technique for z -scanning-free SRS 3D imaging.

2.2 Development of PM-SRST System

Figure 1(a) illustrates the schematic of the PM-SRST system developed for 3D chemical imaging. A 100-fs laser (InSight, Spectra Physics) operating at 80 MHz repetition rates provides dual color outputs: a fixed 1041 nm beam (Stokes), and a tunable (680 to 1300 nm) beam (pump) for generating an SRS signal. The Stokes beam is modulated at 20 MHz by an electro-optic modulator (EOM) and then projected onto an SLM (HCA512-780-940, Meadowlark Optics). After modulating the phase patterns of the Stokes beam by the SLM, the +1st-order of the diffracted Stokes light is selected for SRS imaging, while the other orders of the diffracted beams are blocked by an aperture. For the pump path, the beam is converted into a Bessel beam after passing through a 0.5 deg axicon (AX2505, Thorlabs). Then the Bessel pump and Gaussian Stokes beams are combined by a dichroic mirror (DMLP900R, Thorlabs) and

coupled into a laser-scanning microscope (MPM-4R, Thorlabs) with a galvo-scanner (GVSM002, Thorlabs), and then focused onto the sample with a high NA objective lens (CFI75 APOCHROMAT 25XW MP 1300, NA = 1.1, Nikon). A high NA condenser (CC Achromat/Aplanat, NA = 1.4, Nikon) is used for collecting forward SRS emission from the sample. In the detection path, the Stokes beam is spectrally removed by using a bandpass filter (795/75, Semrock), while the modulated pump beam is detected by a large-area photodiode (FDS1010, Thorlabs) with a lock-in amplifier for demodulating the stimulated Raman loss signal from the pump beam for SRS 3D imaging.

Figure 1(b) shows the schematic of the working principle of the PM-SRST technique. To achieve the depth-resolved SRS 3D imaging, the pump beam is a needle Bessel beam in the sample. The axial position of the Gaussian Stokes spot is manipulated along the needle Bessel pump beam by controlling the divergent angles of the incident Gaussian Stokes beam with the SLM before entering the objective lens. The modulated phase patterns corresponding to specific depths [Eq. (5)] are generated [Fig. S1(a) in the [Supplementary Material](#)] and varied on the SLM for 3D chemical imaging. For example, the raw SRS images of polystyrene (PS) beads are acquired at $z = 0 \mu\text{m}$, $4 \mu\text{m}$, and $8 \mu\text{m}$, respectively [Fig. 1(c)], illustrating the depth-sectioning capability of PM-SRST experimentally.

2.3 Sample Preparation

The $10 \mu\text{m}$ PS beads (17136, Polysciences) embedded in 2% agarose gel phantoms are used for 3D imaging

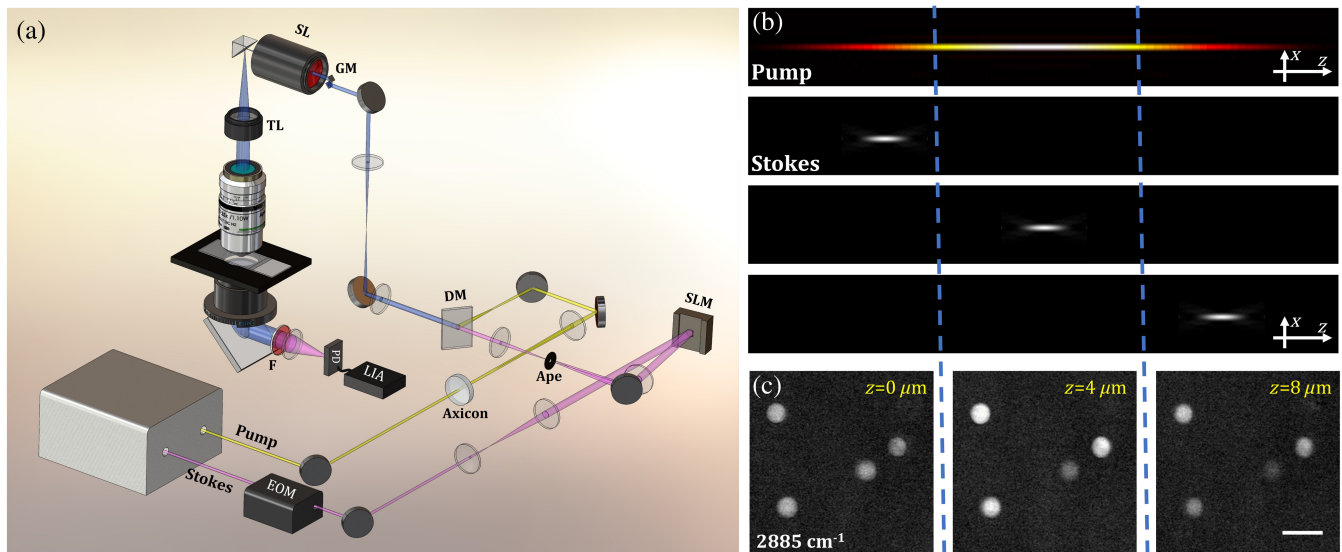


Fig. 1 (a) Schematic of PM-SRST system for 3D chemical imaging. EOM, electro-optical modulator; SLM, spatial light modulator; Ape, aperture; DM, dichroic mirror; GM, galvo mirror; SL, scan lens; TL, tube lens; F, filter; LIA, lock-in amplifier; PD, photodiode. (b) Schematic of the working principle of PM-SRST. The pump beam is converted into a Bessel beam, and the Stokes beam is focused into the sample. The depth-resolved SRS image is achieved by manipulating the axial position of the focused Gaussian Stokes beam and the overlapping with the needle Bessel pump beam at different depths by SLM. (c) Raw SRS images of $10 \mu\text{m}$ PS beads (2885 cm^{-1} of CH_2 asymmetric stretching) measured at $z = 0 \mu\text{m}$, $4 \mu\text{m}$, and $8 \mu\text{m}$, respectively, by PM-SRST. Scale bar $20 \mu\text{m}$. 256×256 pixels for bead imaging. Average powers of the pump and Stokes beams are 5 and 40 mW on the sample.

($\sim 2 \times 10^7$ particles/mL). The $4.5 \mu\text{m}$ PS bead suspension (17135, Polysciences, diluted 10 times with water) is dropped onto the microscope slides with a single well (MS15C1, Thorlabs) for SRS monitoring of Brownian motion. The 500 nm fluorescent beads (19507, Polysciences) are fixed on the microscope slides for measuring the intensity distributions of the focused Gaussian Stokes beam and the needle Bessel–Stokes beam in the $x-y$ and $x-z$ planes. The 500 nm PS beads (07307, Polysciences) are fixed on microscope slides for the assessment of the point spread function (PSF) (i.e., lateral resolution) of the PM-SRST technique.

For imaging the plant's root, the seed of choy sum is cultured in the soil containing okara-based hydrogels¹⁷ under the conditions of the temperature of $25^\circ\text{C} \pm 2^\circ\text{C}/22^\circ\text{C} \pm 2^\circ\text{C}$ (light/dark) with RGB LED lights [$\sim 160 \mu\text{mol}/(\text{m}^2 \cdot \text{s})$ under 12 h light on/12 h light-off illumination] for about half of a month, and the intact root of the plant is cut by surgical blades and fixed on the microscope slide with nail polish. Then $20 \mu\text{L}$ D_2O (151882-10X0.6ML, Sigma) is dropped onto the root for SRST monitoring of the diffusion and uptake processes of D_2O in the plant root.

The breast cancer cell line (MCF-7) is cultured in the medium containing a high-glucose Dulbecco's modified eagle medium (DMEM), 1% penicillin-streptomycin, and 10% FBS. Cells are subcultured and plated on a bottom glass (MatTek Co., Ashland, MA) for three days in the incubator. Before SRST imaging, the cells are washed twice with PBS to remove excess media. About $2 \mu\text{L}$ 100% acetic acid is dropped into 0.5 mL PBS to treat the cells.

The fresh porcine skin and brain (purchased from the local supermarket) tissue slides with tissue thicknesses of ~ 510 and $340 \mu\text{m}$, respectively, are prepared by using surgical blades and sandwiched in between the coverslips for SRST imaging.

2.4 SRS Imaging Parameters

The time constant of $2 \mu\text{s}$ in the lock-in amplifier is used for SRS imaging. A 2D raster scan rate of 51.2 Hz (pixel dwell time of $2.8 \mu\text{s}$, pixel numbers of 64×64) is used for monitoring the Brownian motion of PS beads in water. For other larger image sizes (pixel numbers of 256×256), a typical 2D raster scan rate of 3.5 Hz (pixel dwell time of $2.8 \mu\text{s}$) is employed in PM-SRST and conventional SRS imaging. The wavelengths of the pump and Stokes beams are 800 and 1041 nm, respectively.

2.5 3D Image Acquisition and Reconstruction

For rapid SRST 3D imaging, the SLM is triggered and synchronized by the microscope scanning module. The phase patterns generated (Fig. S1 in the [Supplementary Material](#)) are projected on the SLM (operating at 60 Hz refresh rate) for acquiring the 2D images at the corresponding depths. A series of 2D images are used to reconstruct 3D volume with ImageJ. For comparison purposes, the conventional point-scan SRS (C-SRS) 3D imaging is also acquired by using a motorized vertical translation stage (switching rate of 10 Hz, KVS30, Thorlabs) to move the sample step-by-step along the z axis.

2.6 Estimations of Spatial Resolution and Light Penetration Depth of PM-SRST

The lateral resolutions of the Gaussian pump and Stokes beam are calculated by $\sigma_p = \frac{0.61\lambda_p}{\text{NA}}$ and $\sigma_s = \frac{0.61\lambda_s}{\text{NA}}$, respectively, where

the λ_p and λ_s are the wavelengths of the pump and Stokes beams, respectively. NA is the numerical aperture. The PSF (main lobe) of the Bessel pump beam is calculated by $\beta = \frac{0.382\lambda_p}{\text{NA}}$ ¹⁸. The lateral resolution of the SRS imaging technique is determined by the superposition of the pump and Stokes beams. Hence, the lateral resolutions of PM-SRST and C-SRS imaging are calculated by $1/\sqrt{1/(\beta)^2 + 1/(\sigma_s)^2}$ and $1/\sqrt{1/(\sigma_p)^2 + 1/(\sigma_s)^2}$, respectively¹⁴. With the use of $\lambda_p = 800 \text{ nm}$, $\lambda_s = 1041 \text{ nm}$ and $\text{NA} = 0.45$ in this study, the lateral resolution of PM-SRST is calculated to be $\sim 0.61 \mu\text{m}$, while the lateral resolution of C-SRS is $\sim 0.86 \mu\text{m}$. In theory, PM-SRST provides ~ 1.4 -fold improvement in lateral resolution as compared to the C-SRS imaging. The axial resolution of the Gaussian pump and Stokes beam can be calculated by $\gamma_p = \frac{2\lambda_p}{\text{NA}^2}$ and $\gamma_s = \frac{2\lambda_s}{\text{NA}^2}$, respectively. Therefore, the axial PSF of C-SRS is calculated to be $6.3 \mu\text{m}$ using $1/\sqrt{1/(\gamma_p)^2 + 1/(\gamma_s)^2}$ ($\text{NA} = 0.45$), while the axial resolution of PM-SRST is equivalent to the axial PSF of the Gaussian Stokes beam, which is $10.3 \mu\text{m}$. In theory, the axial resolution of C-SRS is ~ 1.6 -fold better than that of PM-SRST. Note that the Gaussian function is employed to fit the intensity distribution of 500 nm PS beads (Fig. 2), in which the full width at half-maximum (FWHM) of the fit curve stands for the resolution of PM-SRST and C-SRS techniques.

The exponential decay function $I = I_0 \exp(-\frac{z}{\delta})$ is used for the calculation of penetration depth, where I_0 and I are the average SRS intensities at the surface and depth z , respectively. δ is the penetration depth, when the SRS intensity I is dropped by $1/e$ of the incident light intensity I_0 .

2.7 Method for the Diffusion Rate Estimation

For estimating the concentration variations of D_2O with time in the plant root [Fig. 6(g)], the water diffusion and uptake model, $C_s = C_0[1 - \exp(-2\frac{\alpha}{R}t)]$ is used¹⁹, where C_s is the water concentration in the root and C_0 is the one at the root surface. The α is the diffusion permeability across the membrane of the cortex cell in the apoplast of the root. R is defined as the thickness of the cortex, corresponding to the step size ($4 \mu\text{m}$) in PM-SRST.

2.8 Definition of Average SRS Intensity, Diameter, and Volume Size of Nucleus in Cancer Cells

To assess the biochemical variations in cancer cells subjected to acetic acid stimulant, the pixel intensity averaging is performed at each depth to derive the average SRS intensity of the cytoplasm within a single cell by excluding the nucleus region. Similarly, the average pixel intensity of the nucleus at each depth is used for calculating the average SRS intensity of the nucleus. The intensity of nucleus is fit with a Gaussian function, and the FWHM of the fit curve is used to estimate the diameter of nucleus. The volume size of nucleus is calculated by multiplying the nucleus area at each depth by the axial step size used.

3 Results

3.1 PM-SRST System Characterization

Figures 2(a)–2(d) show the comparison of the lateral and axial resolutions between the PM-SRST and C-SRS imaging on a

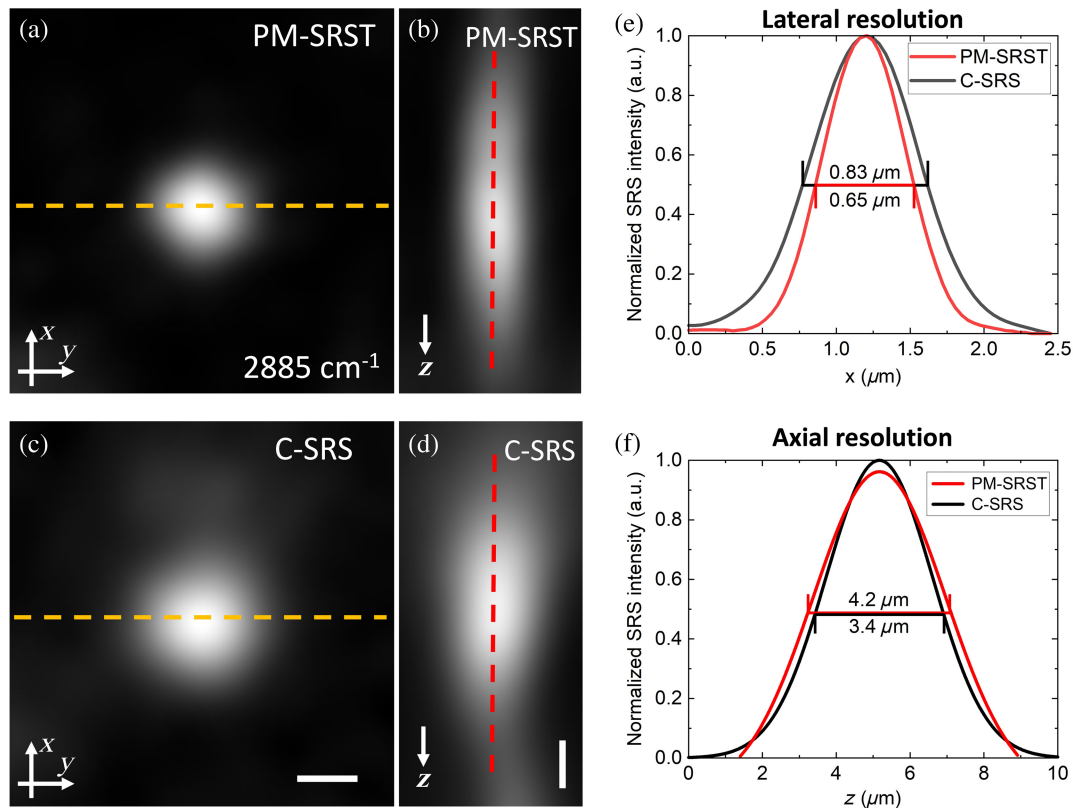


Fig. 2 (a) and (c) Lateral SRS images (2885 cm^{-1} of CH_2 asymmetric stretching) of the 500 nm PS bead measured by PM-SRST and C-SRS imaging. Scale bar: 500 nm . (b) and (d) Axial SRS images of the 500 nm PS bead measured by PM-SRST and C-SRS imaging. Scale bar: $1\text{ }\mu\text{m}$. 256×256 pixels for beads imaging. Average powers of the pump beam are 10 mW for PM-SRST and 2 mW for C-SRS, with the Stokes beam power of 35 mW on the beads. (e) SRS intensity distribution along the dashed line in (a) and (c) with the estimated FWHMs for PM-SRST ($0.65\text{ }\mu\text{m}$) and C-SRS imaging ($0.83\text{ }\mu\text{m}$). (f) SRS intensity distribution along the dashed red line in (b) and (d) with the estimated FWHMs for PM-SRST ($4.2\text{ }\mu\text{m}$) and C-SRS imaging ($3.4\text{ }\mu\text{m}$).

500 nm PS bead. The corresponding lateral resolutions for PM-SRST and C-SRS imaging are 0.65 and $0.83\text{ }\mu\text{m}$, respectively [Fig. 2(e)], giving a ~ 1.3 -fold improvement in lateral resolution achieved by PM-SRST. The axial resolution of PM-SRST is $\sim 4.2\text{ }\mu\text{m}$ [Fig. 2(f)], which is slightly lower than that of C-SRS imaging ($3.4\text{ }\mu\text{m}$). The experimental measurement result above is close to the theoretical values (Sec. 2.6). The slight discrepancies in spatial resolutions between the experiment and theoretical calculations may be due to the slightly lower NA for the pump and Stokes beams used in PM-SRST experiments.

We also compare the light-penetration depth of PM-SRST with C-SRS imaging by measuring SRS images of the $10\text{ }\mu\text{m}$ PS beads in agarose gel phantoms [Fig. 3(a)]. The z -scanning-free PM-SRST imaging shows almost the same PS beads 3D distributions in the gel phantom as those in conventional mechanical point-scanning SRS imaging, but the SRS signal from the deeper bead areas in PM-SRST is much stronger than that in C-SRS (e.g., the bead pointed by the yellow arrow in the deeper area of the tissue phantom is much brighter in PM-SRST compared to that in C-SRS). To quantitatively analyze the

imaging penetration depth by PM-SRST, Fig. 3(b) shows the normalized SRS intensities of the beads along the depth z in PM-SRST as compared to C-SRS imaging. The plots are fit by the exponential decay function (refer to Sec. 2.6). The penetration depth $\delta = 155.3\text{ }\mu\text{m}$ [95% confidence interval: ($86\text{ }\mu\text{m}$, $224.5\text{ }\mu\text{m}$)] is obtained for PM-SRST, while $\delta = 78.5\text{ }\mu\text{m}$ [95% confidence interval: ($56.6\text{ }\mu\text{m}$, $100.5\text{ }\mu\text{m}$)] for C-SRS. The PM-SRST technique provides \sim twofold improvement in penetration depth in polymer beads phantom as compared to C-SRS imaging, affirming the potential of PM-SRST for deeper tissue 3D imaging.

To demonstrate the rapid 3D imaging capabilities of PM-SRST, we monitor the 3D Brownian motion of PS beads in water. Figure 3(c) displays a series of snapshot SRS 3D images of the moving beads in water captured at the 3D volume rate of 8.5 Hz (in a 118 ms time interval) (see Video 1 and Fig. S1 in Supplementary Material for details) without the image blurring of the beads traced. We also measure the 3D Brownian motion of $\sim 2.3\text{ }\mu\text{m/s}$ of the bead, as indicated with a solid yellow arrow in Fig. 3(c), which is in agreement with the theoretical prediction of $2.2\text{ }\mu\text{m/s}$ (with a time of 0.118 s and temperature

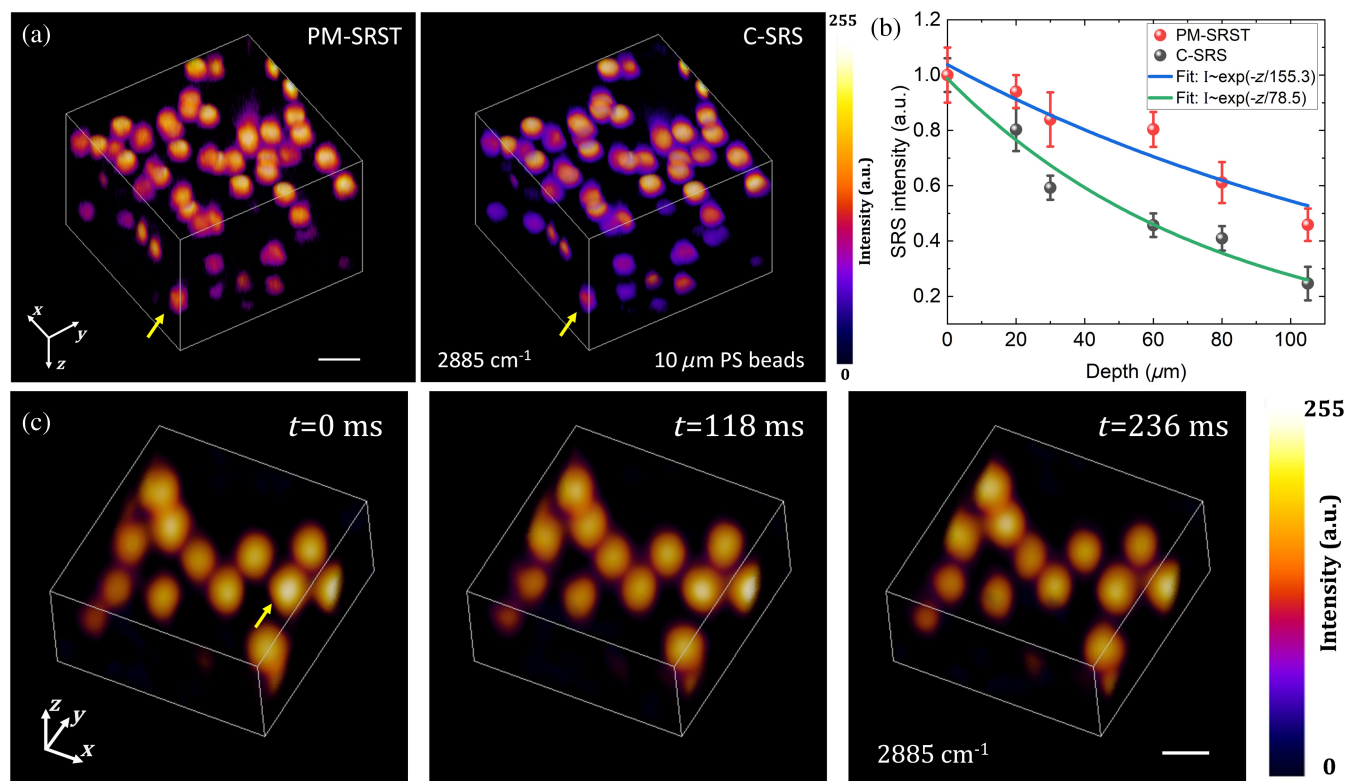


Fig. 3 (a) $10\ \mu\text{m}$ PS beads volume in gel phantom ($2885\ \text{cm}^{-1}$ of CH_2 asymmetric stretching) measured by PM-SRST and C-SRS imaging. The yellow solid arrows indicate the brighter PS bead at the deep position obtained by PM-SRST as compared to C-SRS. Scale bar: $20\ \mu\text{m}$. Image volume: $92.3\ \mu\text{m} \times 92.3\ \mu\text{m} \times 125\ \mu\text{m}$. 256×256 pixels for 2D scanning, axial step size of $5\ \mu\text{m}$. Total 26 depths and 7.4 s time for one 3D volume acquisition. Average powers of the pump beam are 15 mW for PM-SRST and 2 mW for C-SRS, with the Stokes beam power of 30 mW on the beads. (b) Comparison of the normalized SRS intensities of PS beads at different depths by PM-SRST and C-SRS techniques. The SRS intensities of the beads at different depths are normalized to the intensity at the top layer (i.e., $z = 0$) for better comparison. (c) Dynamic 3D SRS images ($2885\ \text{cm}^{-1}$ of CH_2 asymmetric stretching) of $4.5\ \mu\text{m}$ PS beads in water. Scale bar: $5\ \mu\text{m}$. Image volume: $23.08\ \mu\text{m} \times 23.08\ \mu\text{m} \times 20\ \mu\text{m}$. 64×64 pixels for 2D scanning, axial step size of $4\ \mu\text{m}$. Total six depths and 0.118 s acquisition time for obtaining one 3D volume (8.5 Hz). Average powers of the pump and Stokes beams are 8 and 40 mW, respectively, on the beads (Video 1, mp4, 630 KB [URL: <https://doi.org/10.1117/1.AP.6.2.026001.s1>]).

of 293 K calculated with Stokes–Einstein equation²⁰), substantiating the potential of PM-SRST for 3D dynamic chemical imaging.

3.2 Monitoring of Diffusion and Uptake Processes of D_2O into the Plant Roots by PM-SRST

We have applied this rapid PM-SRST technique to observe the 3D diffusion and uptake processes of D_2O in the fresh plant root. Figure 4(a) presents the 3D dynamic process of D_2O ($2530\ \text{cm}^{-1}$ of the O–D chemical bond in the silent region) in the root captured by the PM-SRST within 5.84 s (Video 2). For the comparison purpose, Fig. 4(b) shows the SRS image ($2530\ \text{cm}^{-1}$) of the same tissue volume by PM-SRST in the absence of D_2O as a control. To better visualize the spatial distribution of D_2O within the plant root, an SRS 3D image of the root at $2885\ \text{cm}^{-1}$ is displayed in Fig. 4(c) [as exemplified in Fig. 4(d)]. Figure 4(e) shows the linear relationship between

the SRS intensity and the concentration of D_2O for determining the distribution of D_2O in the plant root [Fig. 4(i)]. Additionally, Fig. 4(f) depicts the variation of SRS intensity along the z axis for the intensity and concentration calibration of D_2O in Figs. 4(g) and 4(i). The SRS intensities of D_2O at each depth in the root are analyzed as shown in Fig. 4(g), showing an exponential increase over time. The plots fit with the water diffusion and uptake equation (refer to Sec. 2.7) in Fig. 4(g), and the diffusion permeabilities of D_2O (1.6 to $2.5\ \mu\text{m}/\text{s}$) are calculated at different depths of the root [Fig. 4(h)]. The results reveal that the deeper regions of the plant's root exhibit a more rapid attainment of equilibrium concentration for D_2O . Furthermore, we estimate the concentration change of D_2O over time in the plant root [Fig. 4(i)]. Notably, the variations of the D_2O concentration versus the plant root's depth at $t = 4.38\ \text{s}$ and $t = 5.84\ \text{s}$ exhibit a consistent trend, suggesting the rapid establishment of a dynamic equilibrium for D_2O diffusion in the plant roots.

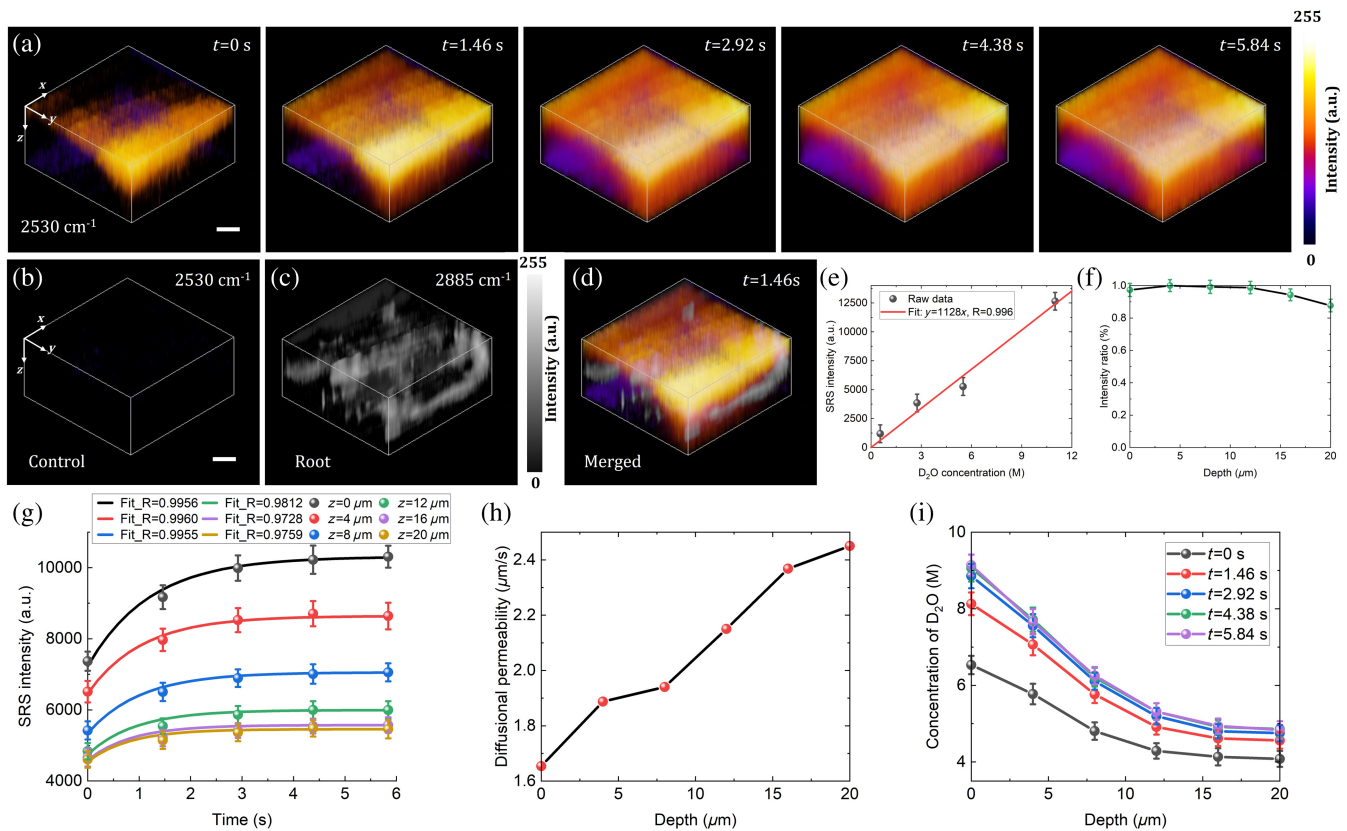


Fig. 4 (a) 3D diffusion dynamics of D_2O (SRS at 2530 cm^{-1} of O-D chemical bond) into the plant's root over time by PM-SRST. Scale bar: $10\ \mu\text{m}$. Image volume: $46.15\ \mu\text{m} \times 46.15\ \mu\text{m} \times 20\ \mu\text{m}$. 256×256 pixels for 2D scanning, axial step size of $4\ \mu\text{m}$. Total six depths and 1.46 s acquisition time for one 3D volume. Average powers of 11 mW (pump beam 824 nm) and 40 mW (Stokes beam) used for SRS imaging of D_2O . (b) and (c) The 3D images of the root at 2530 cm^{-1} (pump beam is set as 824 nm) and 2885 cm^{-1} (CH_2 asymmetric stretching). Scale bar: $10\ \mu\text{m}$. Image volume: $46.15\ \mu\text{m} \times 46.15\ \mu\text{m} \times 20\ \mu\text{m}$. Average powers of 10 mW (pump beam 800 nm) and 40 mW (Stokes beam) on the root. (d) Merged image of the root and the distribution of D_2O at $t = 1.46\text{ s}$. (e) Linear relationship of SRS intensity versus D_2O concentration. (f) SRS intensity at each depth for the intensity and concentration calibration of D_2O in (g) and (i). (g) SRS signal temporal variations and fit results with correlation coefficients (R) at different root depths. (h) Diffusion permeability of D_2O versus tissue depth calculated from (g). (i) Concentration change of D_2O with tissue depth (Video 2, mp4, 85.6 KB [URL: <https://doi.org/10.1177/1.AP.6.2.026001.s2>]).

3.3 Visualization of Biochemical Variations of Live Breast Cancer Cells Subjected to Acetic Acid by PM-SRST

We have also utilized PM-SRST to visualize the rapid biochemical variation of breast cancer cells (MCF-7) subjected to acetic acid stimulants. Figure 5(a) shows the snapshot 3D time-lapse SRS images (2935 cm^{-1}) of the cells captured by PM-SRST (Video 3). An increasing trend in SRS intensity within the nucleus is observed (indicated by a red solid arrow). To gain deeper insights into this phenomenon, we investigate the temporal evolution of nucleus volume versus volume-averaging SRS intensity, as depicted in Fig. 5(c). The increase in SRS intensity within the nucleus observed coincides with a concurrent reduction in nucleus volume size, indicating a direct correlation between the enhanced SRS signal and the nucleus shrinkage in response to the acetic acid stimuli within seconds.

We also analyze the SRS intensity variation in the cytoplasm over time [Fig. 5(d)]. Initially, the SRS signals show an

increasing trend but subsequently decline at each depth within the cytoplasm. These observations can be attributed to the localized concentration increase of biochemicals resulting from the rapid cell contraction and subsequent degradation of lipids/proteins inside the cytoplasm in cells.

To further investigate the biochemical variations in the cells, Fig. 5(b) depicts the SRS 3D dynamic process of the cells at 2845 cm^{-1} captured by PM-SRST (Video 4). Figure 5(e) shows the change in SRS intensity over time inside the cytoplasm. We find that the SRS intensity at 2845 cm^{-1} consistently increases during the stimulus, probably due to the localized intensity enhancement [indicated by the black solid arrows in Fig. 5(b)] caused by the cell shrinkage following exposure to acetic acid. Consequently, by comparing the SRS intensity variations at 2845 cm^{-1} (associated with CH_2 symmetric stretching of lipids) and 2935 cm^{-1} (CH_3 stretching of lipids and proteins) in cells, we can infer the degradation of proteins within the cytoplasm of live cells during acetic acid stimuli.

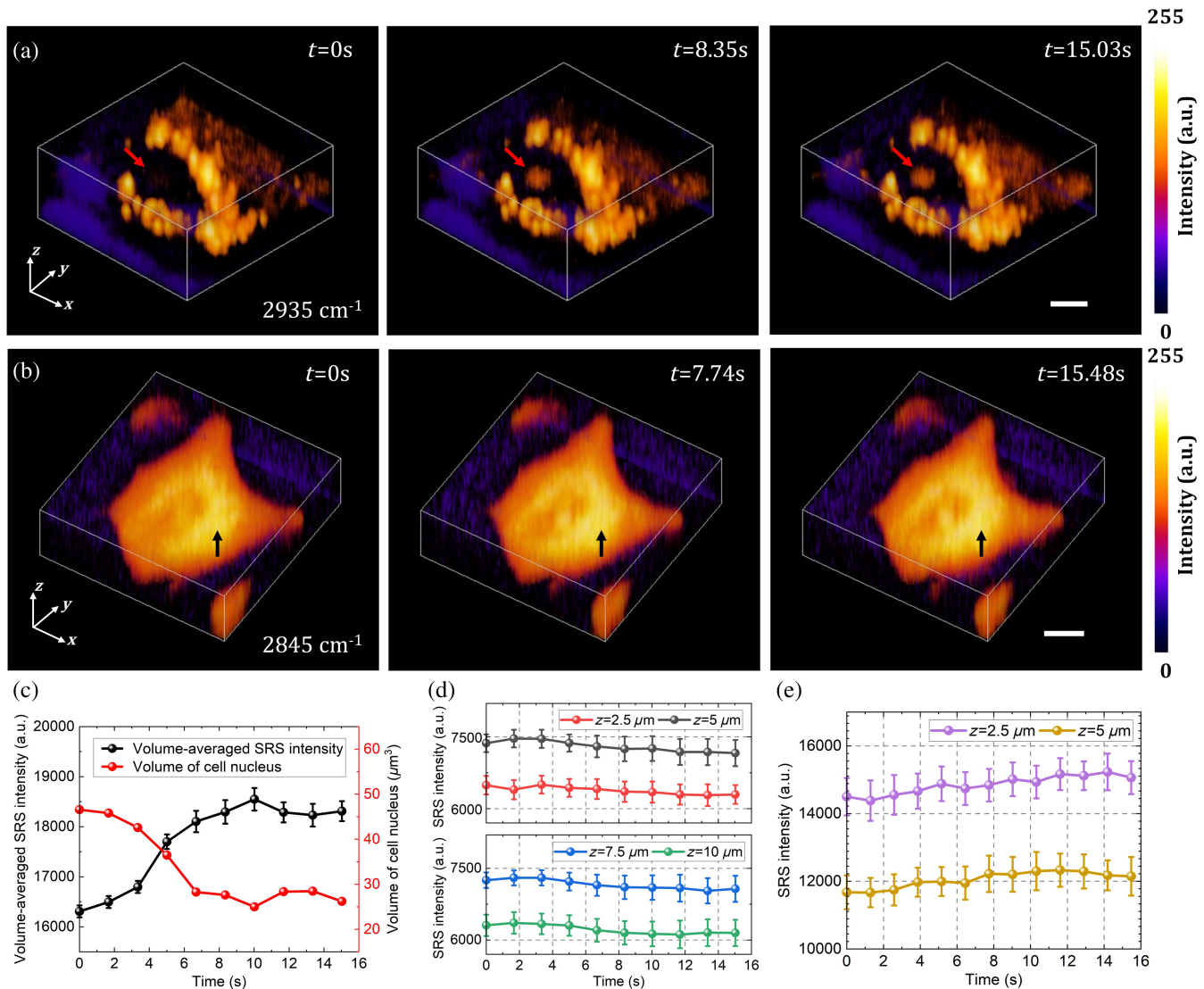


Fig. 5 (a) 3D SRS dynamics of MCF-7 cells (2935 cm^{-1} of CH_3 stretching of lipids and proteins) subjected to 0.4% acetic acid observed by PM-SRST. Red arrows indicate the intensity variation of the nucleus over time. Scale bar: $5\text{ }\mu\text{m}$. Image volume: $23.08\text{ }\mu\text{m} \times 23.08\text{ }\mu\text{m} \times 15\text{ }\mu\text{m}$. 256×256 pixels for 2D scanning, axial step size of $2.5\text{ }\mu\text{m}$. Total seven depths and 1.67 s acquisition time for obtaining one 3D volume. Average powers of the pump (797 nm) and Stokes beams are 10 and 40 mW on the cells. (b) Dynamic variations of MCF-7 cells (2845 cm^{-1} of CH_2 symmetric stretching of lipids; pump beam is set as 805 nm) exposed to 0.4% acetic acid by PM-SRST. Black arrows indicate the intensity variation inside the cytoplasm over time. Scale bar: $10\text{ }\mu\text{m}$. Image volume: $46.13\text{ }\mu\text{m} \times 46.13\text{ }\mu\text{m} \times 7.5\text{ }\mu\text{m}$. 256×256 pixels for 2D scanning; axial step size of $2.5\text{ }\mu\text{m}$. Total four depths and 1.29 s acquisition time for one 3D volume. Average powers of the pump (804 nm) and Stokes beams are 10 and 40 mW, respectively, on the cells. (c) SRS intensity change of the nucleus (black dot line) and the reduction of nucleus volume (red dotted line) over time for the cell in (a). (d) and (e) SRS intensity variation in the cytoplasm versus time at different depths for the cells in (a) and (b), respectively (Video 3, mp4, 165 KB [URL: <https://doi.org/10.1117/1.AP.6.2.026001.s3>] and Video 4, mp4, 217 KB [URL: <https://doi.org/10.1117/1.AP.6.2.026001.s4>]).

3.4 Assessment of Deeper Penetration Capability of PM-SRST in Biotissues

We have further validated the capability of PM-SRST technique to improve the imaging depth in highly scattering biotissues (e.g., porcine skin and brain tissue) compared to C-SRS

imaging. Figs. 6(a) and 6(b) present the SRS 3D images of porcine skin tissue captured by PM-SRST and C-SRS, confirming a higher SRS intensity observed from deeper regions of the tissue with the PM-SRST technique. To better visualize the improvement in penetration depth, Figs. 6(c) and 6(d) display the $x-z$ plane of the 3D images in Figs. 6(a) and 6(b), showing the

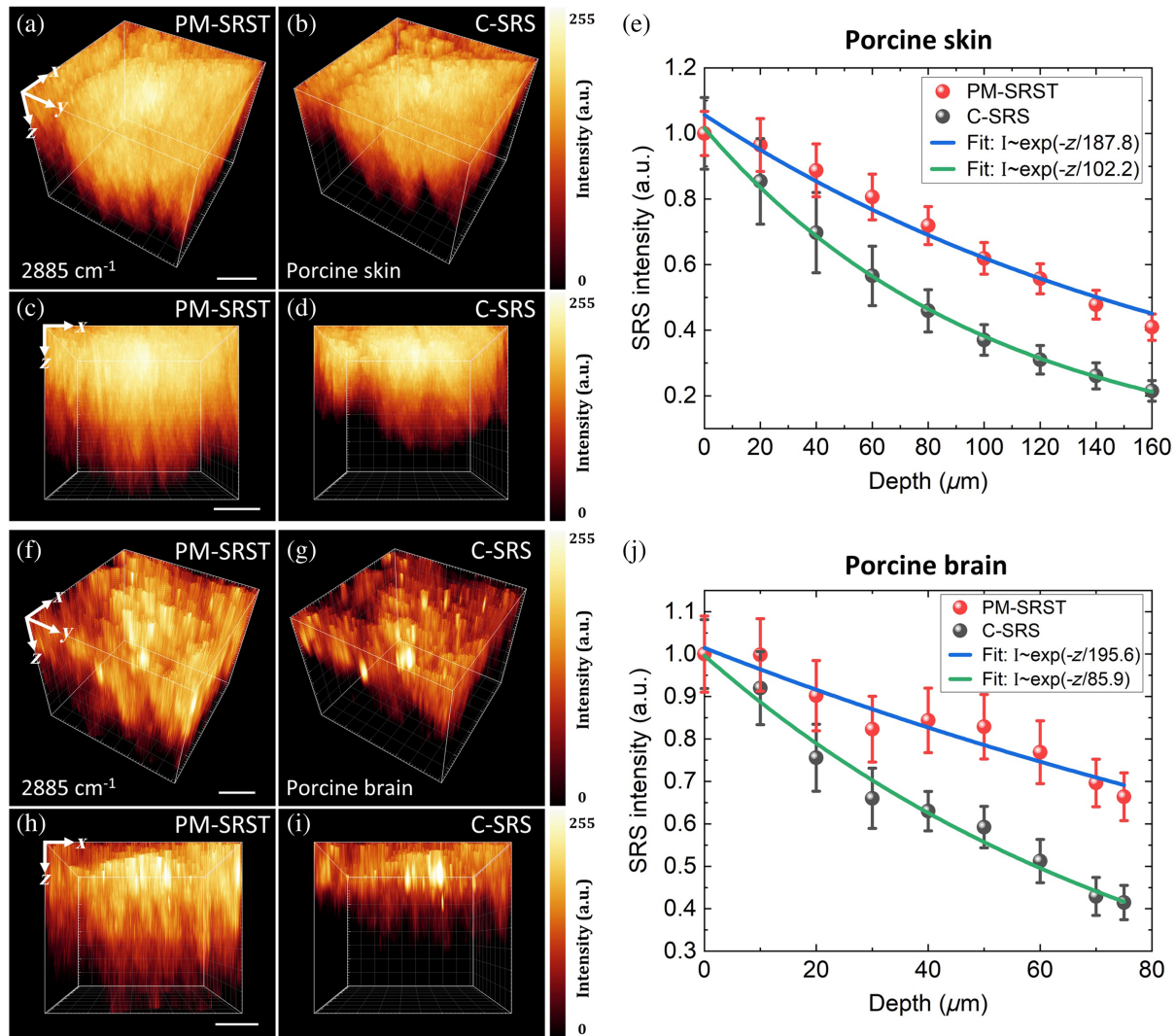


Fig. 6 (a) and (b) SRS 3D images (2885 cm^{-1} of CH_2 asymmetric stretching of lipids) of the porcine skin tissue obtained using PM-SRST and C-SRS techniques. Scale bar: $40\text{ }\mu\text{m}$. Image volume: $184.6\text{ }\mu\text{m} \times 184.6\text{ }\mu\text{m} \times 160\text{ }\mu\text{m}$. 256×256 pixels for 2D scanning, axial step size of $5\text{ }\mu\text{m}$. Total 33 depths and 9.4 s acquisition time for getting one 3D volume. Average powers of the pump beam are 2.5 mW for PM-SRST and 0.5 mW for C-SRS, with the Stokes beam power of 13.5 mW on porcine skin. (c) and (d) $x - z$ plane view of (a) and (b). Scale bar: $40\text{ }\mu\text{m}$. (e) Comparison of SRS intensities at different depths in porcine skin tissue using PM-SRST and C-SRS techniques. The SRS intensities at each depth in porcine skin are normalized to the intensity in the top-layer ($z = 0\text{ }\mu\text{m}$) for imaging performance comparison between PM-SRST and C-SRS. (f) and (g) SRS 3D images (2885 cm^{-1}) of the porcine brain tissue captured by PM-SRST and C-SRS imaging. Scale bar: $20\text{ }\mu\text{m}$. Image volume: $92.3\text{ }\mu\text{m} \times 92.3\text{ }\mu\text{m} \times 80\text{ }\mu\text{m}$. 256×256 pixels for 2D scanning; axial step size of $5\text{ }\mu\text{m}$. Total 17 depths and 4.9 s acquisition time for one 3D volume. Average powers of the pump beam are 6 mW for PM-SRST and 1 mW for C-SRS, with the Stokes beam power of 33 mW on porcine brain. (h) and (i) $x - z$ plane view of (f) and (g). Scale bar: $20\text{ }\mu\text{m}$. (j) Comparison of the SRS intensities at each tissue depth in porcine brain using PM-SRST and C-SRS. The SRS intensities at each depth in the porcine brain are normalized to the intensity in the top layer ($z = 0\text{ }\mu\text{m}$) for the imaging performance comparison between PM-SRST and C-SRS.

enhanced imaging depth achieved by PM-SRST in comparison with C-SRS. Figure 6(e) shows the measured average SRS intensities at different tissue depths that are normalized to the average SRS intensity (all pixel intensities) at the tissue surface ($z = 0\text{ }\mu\text{m}$). The fitting curves using the exponential decay function (refer to Sec. 2.6) indicate that the penetration depth

in porcine skin by PM-SRST is $\sim 187.8\text{ }\mu\text{m}$, giving \sim twofold improvement in imaging depth compared to C-SRS imaging ($102.2\text{ }\mu\text{m}$). We have also compared the imaging depths between PM-SRST and C-SRS imaging in even stronger scattering porcine brain tissue.²¹ Figures 6(f) and 6(g) present the 3D images of brain tissue along with $x - z$ plane image [Figs. 6(h) and 6(i)],

confirming the significant improvement in penetration depth achieved by PM-SRST. The SRS intensity profiles along the z direction in Fig. 6(j) show that the penetration depth for PM-SRST in brain tissue is $\sim 195.6 \mu\text{m}$, giving rise to a 2.3-fold improvement in imaging depth as compared to C-SRS imaging ($85.9 \mu\text{m}$). Thus, PM-SRST exhibits the enhanced penetration capability for achieving deeper 3D chemical imaging in biological tissues. The slight variations in the degree of improvement in imaging depths among different tissue samples may be attributed to the varying scattering effects encountered in different types of tissues [e.g., porcine skin (scattering coefficients 13 cm^{-1} for 800 nm and 8 cm^{-1} for 1041 nm) and brain tissue (19.5 cm^{-1} for 800 nm and 14 cm^{-1} for 1041 nm)]²¹.

4 Discussion

Conventional SRS 3D imaging coupled with mechanical z scanning encounters the challenges in inertia artifacts and slow imaging speed in tissue and cells.¹² The strong scattering effect in turbid media (e.g., tissue) also dramatically attenuates the light-propagating intensity in deeper tissue regions, limiting the imaging depth.²² To tackle these issues, we have developed a unique PM-SRST technique that enables rapid 3D chemical imaging by electronically tuning the superpositions of the focused Gaussian–Stokes beam along the needle Bessel pump beam without the need for mechanical z scanning. The fast 3D imaging capability is achieved by rapidly controlling the axial positioning of the Stokes beam with a phase modulation device. We use the SLM as a phase modulator to evaluate the imaging speed of PM-SRST by monitoring the 3D Brownian motion of PS beads in water [Fig. 3(c)], in which the 3D volume rate of 8.5 Hz [i.e., 118 ms time interval, six phase patterns, Fig. S1(a) in the [Supplementary Material](#)] can be achieved. Compared with the deformable mirror-based volumetric SRS imaging,²³ PM-SRST shows a remarkable superiority with millisecond time intervals, confirming the advantages of electronically-controlled phase modulations for improving depth-resolved SRS 3D imaging speed. To acquire more sectioning images along the z axis, a faster phase modulation device could be employed for PM-SRST. Compared to an electrically tunable lens (~ 100 Hz frame rate²⁴) or a tunable acoustic gradient index of refraction lens (constrained dwelling capacity²⁵) with device-induced spherical and high-order aberration,²⁶ the microelectromechanical system (MEMS)-based SLM (kilohertz frame rate)^{24,27} or digital micromirror device (DMD, 4.2 kHz²⁸) could be used to further boost the z -sectioning speed of the PM-SRST technique for video-rate SRS 3D imaging of tissue and cells. PM-SRST also provides a deeper light-penetration depth for 3D chemical imaging in tissue compared to C-SRS imaging. We have experimentally demonstrated a twofold improvement in imaging depth in PS beads phantom by PM-SRST [Figs. 3(a) and 3(b)] compared to C-SRS imaging. To elucidate the reason for this improvement in penetration depth within a highly scattering medium, we estimate the scattering coefficients for the pump beam (33.5 cm^{-1} at 800 nm) and Stokes beam (28.6 cm^{-1} at 1041 nm) based on the Mie scattering model²⁹ [the density of the beads used in the phantom is $\sim 2 \times 10^7$ particles/mL in SRS imaging; see Fig. 3(a)]. Our results indicate a lower scattering for the longer wavelength (1041 nm) in the beads phantoms. As a result, the penetration depth of C-SRS imaging is predominantly constrained by the higher scattering effect of the shorter wavelength pump beam (800 nm). In PM-SRST, we convert the Gaussian pump beam into a nondiffracting Bessel beam, which has been

proven to be a relatively good scattering-resistant property with remarkable resilience to scattering effects in turbid media.^{18,30} Additionally, the utilization of a longer wavelength Stokes beam within the NIR-II window (1000 to 1700 nm) further enhances the capability for deeper tissue imaging compared to the NIR-I window (650 to 950 nm)^{31,32}. Thus, by combining the advantages of the scattering-resilient Bessel pump beam (800 nm) and the longer wavelength of Stokes beam (1041 nm), PM-SRST successfully boosted the SRS 3D imaging depth in bio-tissues [e.g., porcine skin and brain tissue (Fig. 6)]. Compared with the conventional adaptive optics (AO) technique, which is widely used for deep tissue imaging by monitoring the aberration of the light wavefront in the sample with a wavefront sensor and subsequently correcting the beam distortion with DM,³³ PM-SRST achieves an improved imaging depth by using the unique scattering-resilient Bessel pump beam together with NIR-II Stokes beam, enabling the rapid 3D deeper imaging in tissue without the time delay associated with the wavefront detection and compensation in AO. On the other hand, the Bessel pump beam used in PM-SRST provides a 1.6-fold narrower main lobe than that of a Gaussian pump beam (refer to Sec. 2.6). Hence, the PM-SRST technique yields a ~ 1.3 -fold enhancement in lateral resolution compared to C-SRS [Fig. 2(e)]. However, the modulation of the Gaussian Stokes beam in PM-SRST operates under the paraxial condition [Eq. (5)], which may limit the maximum utilization of the tightly focused Stokes beam (e.g., NA 1.1, nonparaxial condition) in PM-SRST. As such, the lateral resolution of PM-SRST at the nonparaxial condition would be constrained to a certain extent. Due to the extended length of the Bessel beam compared to the Gaussian spot, the overlapped portion of the pump and Stokes beams in PM-SRST along the z -axis direction is a bit larger than that of the C-SRS. Consequently, the axial resolution of PM-SRST is slightly compromised in comparison to C-SRS [Fig. 2(f)]. To mitigate this effect for enhancing the spatial resolution, the deconvolution algorithms (e.g., Richardson–Lucy algorithm³⁴) can be incorporated into the PM-SRST technique, offering the potential for rapid superresolution imaging in deep tissue.

The PM-SRST technique presented in this work is fundamentally different from our previously reported Bessel beam-based OBT SRS 3D imaging technique¹⁴ in terms of its working principles and imaging performance. (i) PM-SRST technique works by electronically tuning the focused Gaussian Stokes beam along the needle Bessel pump beam with the SLM, facilitating the direct acquisition of 3D sample information in the spatial or time domain without necessitating the postprocessing procedures. In contrast, OBT operates by encoding the 3D information with Bessel beam beatings after hundreds of varying spatial frequency interval scans (>20 min) in the frequency domain, and the volumetric information is reconstructed through the inverse Fourier transform. (ii) Our two-photon fluorescence (TPF) experiments (refer to Fig. S2 in the [Supplementary Material](#)) show that the tightly focused Gaussian Stokes beam used in PM-SRST is ~ 16 -fold stronger in local laser intensity as compared to the Bessel Stokes beam used in OBT-SRST. Hence, the PM-SRST technique using the Bessel pump beam coupled with the tightly focused Gaussian Stokes excitation scheme can significantly enhance the signal-to-noise ratio (SNR) over OBT-based SRST, achieving a much faster SRS 3D imaging speed in cells and tissue. (iii) Given the similar axial resolutions ($4.2 \mu\text{m}$, NA = 0.45 for PM-SRST;

5.49 μm , NA = 0.54 for OBT), PM-SRST facilitates rapid 3D imaging within 10 s [33 scans of 2D images, 160 μm depth in Figs. 6(a) and 6(b)], and the PM-SRST 3D imaging can be completed even down to 0.118 s (8.5 Hz, laser power of 48 mW), as shown in Fig. 3(c). In contrast, ~ 28.2 min of OBT-SRS 3D imaging time (141 scans of 2D images, maximum 200 μm depth, scanning rates of 12 s, laser power of 100 mW) is required for reconstructing a single 3D volume in OBT 3D imaging.¹⁴ Therefore, PM-SRST significantly boosts the 3D imaging speed with high SNRs and imaging depths for monitoring the dynamic functional and metabolic processes in tissue and cells with a lower incident laser power compared to the Bessel beam-based OBT SRS 3D imaging.

In summary, we have developed a unique PM-SRST technique for rapid label-free 3D chemical imaging in deeper tissue and cells without the need for mechanical z scanning. We demonstrate the ability of PM-SRST technique for rapid dynamic/functional, and morphological 3D imaging in a variety of applications (e.g., Brownian motion monitoring, instant response of breast cancer cells to acetic acid stimuli, diffusion and permeation of D_2O in plant roots). One notes that the z -scanning-free optical sectioning property with the phase control conceived in PM-SRST is universal, which can be easily extended to other imaging modalities for advancing 3D microscopy imaging in biological and biomedical systems. For instance, the current PM-SRST system can be readily adapted for CARS tomography by substituting the photodiode with a photomultiplier tube to capture 3D CARS signals. By utilizing either the pump or Stokes beam alone, the PM-SRST technique can be simplified to facilitate second-/third-harmonic generation tomography, multiphoton tomography, or fluorescence tomography, etc. We anticipate that the PM-SRST technique holds great promise to serve as a rapid z -scanning-free 3D chemical imaging tool for a wide range of label-free biomolecular imaging applications in biology, biochemistry, and biomedicine.

Disclosures

The authors declare no competing interests.

Code and Data Availability

Data underlying the results presented in this paper are not publicly available at this time but may be obtained from the corresponding author upon reasonable request.

Supplementary Materials

See Supplement 1 and Videos 1 to 4 for supporting content.

Acknowledgments

This work was supported by the Academic Research Fund (AcRF)-Tier 2 (A-8000117-01-00) and Tier 1 (R397-000-334-114, R397-000-371-114, and R397-000-378-114) from the Ministry of Education (MOE), the Merlion Fund (WBS R-397-000-356-133), and the National Medical Research Council (NMRC) (A-0009502-01-00 and A-8001143-00-00), Singapore.

References

- G. J. Brakenhoff et al., "Three-dimensional chromatin distribution in neuroblastoma nuclei shown by confocal scanning laser microscopy," *Nature* **317**(6039), 748–749 (1985).
- W. Denk, J. H. Strickler, and W. W. Webb, "Two-photon laser scanning fluorescence microscopy," *Science* **248**(4951), 73–76 (1990).
- X. Chen et al., "Second harmonic generation microscopy for quantitative analysis of collagen fibrillar structure," *Nat. Protoc.* **7**(4), 654–669 (2012).
- P. Nandakumar, A. Kovalev, and A. Volkmer, "Vibrational imaging based on stimulated Raman scattering microscopy," *New J. Phys.* **11**(3), 033026 (2009).
- C. W. Freudiger et al., "Label-free biomedical imaging with high sensitivity by stimulated Raman scattering microscopy," *Science* **322**(5909), 1857–1861 (2008).
- C. M. Tempamy et al., "Multimodal imaging for improved diagnosis and treatment of cancers," *Cancer* **121**(6), 817–827 (2015).
- M. A. Miller and R. Weissleder, "Imaging of anticancer drug action in single cells," *Nat. Rev. Cancer* **17**(7), 399–414 (2017).
- F. Hu, L. Shi, and W. Min, "Biological imaging of chemical bonds by stimulated Raman scattering microscopy," *Nat. Methods* **16**(9), 830–842 (2019).
- L. Streich et al., "High-resolution structural and functional deep brain imaging using adaptive optics three-photon microscopy," *Nat. Methods* **18**(10), 1253–1258 (2021).
- M. Wei et al., "Volumetric chemical imaging by clearing-enhanced stimulated Raman scattering microscopy," *Proc. Natl. Acad. Sci. U. S. A.* **116**(14), 6608–6617 (2019).
- J. X. Cheng and X. S. Xie, "Vibrational spectroscopic imaging of living systems: an emerging platform for biology and medicine," *Science* **350**(6264), aaa8870 (2015).
- J. Wu, N. Ji, and K. K. Tsia, "Speed scaling in multiphoton fluorescence microscopy," *Nat. Photonics* **15**(11), 800–812 (2021).
- X. Chen et al., "Volumetric chemical imaging by stimulated Raman projection microscopy and tomography," *Nat. Commun.* **8**(1), 15117 (2017).
- L. Gong, S. L. Lin, and Z. W. Huang, "Stimulated Raman scattering tomography enables label-free volumetric deep tissue imaging," *Laser Photonics Rev.* **15**(9), 2100069 (2021).
- O. Brzobohatý, T. Čížmár, and P. Zemánek, "High quality quasi-Bessel beam generated by round-tip axicon," *Opt. Express* **16**(17), 12688–12700 (2008).
- A. Nussbaum, "Teaching of advanced geometric optics," *Appl. Opt.* **17**(14), 2128–2129 (1978).
- J. Zhu et al., "Converting okara to superabsorbent hydrogels as soil supplements for enhancing the growth of choy sum (*Brassica* sp.) under water-limited conditions," *ACS Sustain. Chem. Eng.* **8**(25), 9425–9433 (2020).
- K. Huang et al., "Optimization-free superoscillatory lens using phase and amplitude masks," *Laser Photonics Rev.* **8**(1), 152–157 (2014).
- M. Zarebanadkouk et al., "Quantification and modeling of local root water uptake using neutron radiography and deuterated water," *Vadose Zone J.* **11**(3), vzj2011.0196 (2012).
- J. T. Edward, "Molecular volumes and the Stokes-Einstein equation," *J. Chem. Educ.* **47**(4), 261 (1970).
- S. Mosca et al., "Optical characterization of porcine tissues from various organs in the 650–1100 nm range using time-domain diffuse spectroscopy," *Biomed. Opt. Express* **11**(3), 1697–1706 (2020).
- F. O. Fahrbach and A. Rohrbach, "Propagation stability of self-reconstructing Bessel beams enables contrast-enhanced imaging in thick media," *Nat. Commun.* **3**(1), 632 (2012).
- P. Lin et al., "Volumetric chemical imaging *in vivo* by a remote-focusing stimulated Raman scattering microscope," *Opt. Express* **28**(20), 30210–30221 (2020).
- B. H. W. Hendriks, et al., "Electrowetting-based variable-focus lens for miniature systems," *Opt. Rev.* **12**, 255–259 (2005).
- N. T. Ersumo et al., "A micromirror array with annular partitioning for high-speed random-access axial focusing," *Light: Sci. Appl.* **9**(1), 183 (2020).

26. T. Chakraborty et al., "Converting lateral scanning into axial focusing to speed up three-dimensional microscopy," *Light: Sci. Appl.* **9**(1), 165 (2020).
27. Y. Takekawa, Y. Takashima, and Y. Takaki, "Holographic display having a wide viewing zone using a MEMS SLM without pixel pitch reduction," *Opt. Express* **28**(5), 7392–7407 (2020).
28. J. Cheng et al., "High-speed femtosecond laser beam shaping based on binary holography using a digital micromirror device," *Opt. Lett.* **40**(21), 4875–4878 (2015).
29. I. S. Saidi, S. L. Jacques, and F. K. Tittel, "Mie and Rayleigh modeling of visible-light scattering in neonatal skin," *Appl. Opt.* **34**(31), 7410–7418 (1995).
30. F. O. Fahrbach, P. Simon, and A. Rohrbach, "Microscopy with self-reconstructing beams," *Nat. Photonics* **4**(11), 780–785 (2010).
31. J. Cao et al., "Recent progress in NIR-II contrast agent for biological imaging," *Front. Bioeng. Biotechnol.* **7**, 487 (2020).
32. H. Wan et al., "A bright organic NIR-II nanofluorophore for three-dimensional imaging into biological tissues," *Nat. Commun.* **9**(1), 1171 (2018).
33. J. M. Girkin, S. Poland, and A. J. Wright, "Adaptive optics for deeper imaging of biological samples," *Curr. Opin. Biotechnol.* **20**(1), 106–110 (2009).
34. D. A. Fish et al., "Blind deconvolution by means of the Richardson–Lucy algorithm," *J. Opt. Soc. Am. A* **12**(1), 58–65 (1995).

Weiqi Wang received his BS degree in optical information science and technology from Ocean University of China in 2016 and his MSc degree in

instrument science and technology from Tsinghua University, China in 2019. He is currently pursuing his PhD in Optical Bioimaging Laboratory under the supervision of Prof. Zhiwei Huang in the Department of Biomedical Engineering at the National University of Singapore. His research is mainly focused on stimulated Raman scattering tomography development and biological and biomedical applications.

Zhiwei Huang received his PhD from Nanyang Technological University, Singapore in 1999; he is the Director of Optical Bioimaging Laboratory in the Department of Biomedical Engineering, College of Design and Engineering at the National University of Singapore. His major research areas are in the fields of biomedical optics, microscopy, Raman spectroscopy and imaging, particularly centering on the development of super-resolution microscopy and nonlinear optical microscopy imaging techniques (e.g., coherent Raman scattering microscopy, multiphoton microscopy) and their applications in biomolecular imaging, as well as the development of novel fiber-optic Raman spectroscopy and endoscopic imaging, enabling early diagnosis and detection of epithelial precancer and cancer at endoscopy. He pioneered in Raman endoscopy and label-free superresolution bioimaging technologies and published over 120 peer-reviewed articles in leading journals (e.g., *Nature Photonics*, *Gastroenterology*). He has filed over 20 U.S. patents, with 10 licensed for commercialization. His IMDX technique invented was ranked No. 1 among the top 10 medical devices listed in Medica, Germany. He is an elective Fellow of SPIE, the international society for optics and photonics.